

Detection of Adsorbates on Emissive MOF Surfaces with X-ray Photoelectron Spectroscopy

*Jingjing Yan,[†] Alexander D. Carl,[†] John C. MacDonald,[†] Peter Müller,[‡] Ronald L. Grimm,[†] and
Shawn C. Burdette^{†*}*

[†]Department of Chemistry and Biochemistry, Worcester Polytechnic Institute, 100 Institute Road,
Worcester, MA 01609-2280 (USA). E-mail: scburdette@wpi.edu

[‡]Department of Chemistry, Massachusetts Institute of Technology, 77 Massachusetts Avenue,
Cambridge, Massachusetts 02139 (USA).

ABSTRACT

Luminescent metal-organic frameworks (MOFs) have been explored extensively as potential probes for nitroaromatic molecules, which are common constituents of explosive devices. Guest encapsulation within MOF pores is often cited as the prerequisite for emission changes, but the evidence for this signal transduction mechanism is often inadequate. Using the unique bipyridyl ligand AzoAEP (2,2'-bis[N,N'-(4-pyridyl)ethyl]diaminoazobenzene), we constructed two luminescent pillared paddle-wheel Zn²⁺ MOFs using aryl dicarboxylate ligands benzene 1,4-dicarboxylic acid (ABMOF-1) and 1,4-naphthalenedicarboxylic acid (ABMOF-2).

While both MOFs exhibit luminescence, 2,4-dinitrophenol only extinguishes ABMOF-1 emission. Since the size of the pores in ABMOF-1 preclude guest inclusion, we used X-ray photoelectron spectroscopy (XPS) to confirm the surface interaction and obtain insight into the nature of the quenching process. XPS experiments utilized a fluorinated nitroaromatic molecule, 4-trifluoromethyl-2,6-dinitrophenol, that extinguishes ABMOF-1 emission, and verified surface adsorption through a series of angle-resolved (ARXPS) and argon-ion sputter depth profile experiments. By further developing these techniques, we hope to develop a general instrumental approach for distinguishing between the various intermolecular interactions between MOFs and analytes that lead to changes in luminescence.

INTRODUCTION

Luminescent metal-organic frameworks (MOFs) have been used extensively as scaffolds to construct luminescent probes for many difficult-to-detect targets including explosives.¹⁻³ While there are many approaches to induce MOF emission, constructing structures with luminescent struts is the most straightforward design strategy to achieve this goal.^{4,5} Electron-deficient compounds such as nitroaromatic molecules constitute an important class of explosive analytes, and typically quench ligand-centered emission.^{2,6} Charge transfer from the excited fluorophores that constitute the MOF struts to the electron deficient species is the most plausible quenching mechanism in most of these systems.

Emission quenching signals communication between MOF and analyte, but not the specific nature of the interactions. More sophisticated measurements can establish the distance

between fluorophore and quencher, as well as differentiate between inner-sphere and outer-sphere mechanisms; however, these can be complex, time-consuming experiments. Similarly UV-vis spectroscopy⁷ and vibrational spectroscopy⁸ can provide some information about MOF-analyte interactions, but also have inherent limitations.

Both π - π stacking^{6, 9} and electrostatic interactions^{2, 10} have been cited to explain nitroaromatic-MOF interactions. Nitroaromatic molecules can be surface-absorbed in MOFs lacking porosity,^{6, 10} but there are also assertions, often with limited proof, that aromatic analytes enter MOF cavities.¹¹⁻¹⁵ An X-ray crystal structure of a MOF-analyte adduct would provide strong evidence for the nature of these interactions; however, crystalizing supramolecular MOF complexes with well-ordered guests necessary for X-ray analysis can be difficult.^{13, 14} Theoretical modeling of these interactions can also be useful,^{16, 17} but are more convincing in conjunction with direct experimental data. Developing a universally applicable technique to probe MOF-analyte interactions would facilitate the ability to design and optimize MOF structures suitable for luminescent probes with greater selectivity and sensitivity.

X-ray photoelectron spectroscopy (XPS) possesses untapped potential to ascertain whether emission-quenching molecules are adsorbed to the MOF surfaces or possibly internalized within the pores. XPS can determine metal oxidation states in MOFs^{18, 19} and MOF composites,²⁰ as well as quantify catalyst decomposition due to side-reactions.²¹ XPS is sensitive to near-surface chemical environments,²² and angle-resolved XPS (ARXPS) further utilizes the attenuation of sub-surface electrons to quantify surface vs. bulk contributions to a photoelectron spectrum.²³ Given these capabilities, we envisioned developing photoelectron spectroscopic techniques to probe interactions in emissive MOF systems.

Based on our earlier studies making emissive coordination polymers with the azobenzene-based extended bipyridyl ligand AzoAEP (2,2'-bis[N,N'-(4-pyridyl)ethyl]diaminoazobenzene),²⁴ we reasoned that we could also construct luminescent pillared paddle-wheel MOFs with standard dicarboxylate ligands and Zn²⁺. Since the emissive azobenzene fluorophore has a large surface area, we hypothesized that we might be able to access pillared paddle-wheel MOFs with unique structural features, and that various nitroaromatic analytes could either π -stack with AzoAEP units, or engage in electrostatic interactions at the metal sites. Furthermore, we expected fluorinated analogs of nitroaromatic adsorbates could be used to help detail the MOF-analyte interactions owing to the high sensitivity of XPS for fluorine,²⁵ and the absence of interfering signals from the chosen MOF components. XPS also affords the opportunity to utilize angle-resolved techniques as well as argon-ion sputtering to desorb near-interfacial species from the MOF substrate, which could reveal the physical arrangement of the nitrophenol compounds relative to the MOF substrate (i.e. surface adsorbed species vs bulk intercalated guests).

EXPERIMENTAL SECTION

General Procedures. All reagents were purchased and used without further purification. AzoAEP (2,2'-bis[N,N'-(4-pyridyl)ethyl]diaminoazobenzene) was prepared as previously described.²⁴ AzoMOF-2 was prepared and characterized analogously to AzoMOF-1, and the details can be found in the supporting information. ¹H NMR spectra were recorded with a 500 MHz Bruker Biospin NMR instrument. Elemental microanalyses for C, H, and N were performed by Micro Analysis Inc (Wilmington DE). FT-IR spectra were recorded using Bruker

Vertex70 Optics FT-IR spectrometer equipped with a Specac Golden Gate attenuated total reflection (ATR) accessory by collecting 1024 scans over a scan range from 4000 to 400 cm^{-1} at 4 cm^{-1} resolution. Thermogravimetric analysis (TGA) measurements were carried out on a TA Instruments Hi-Res TGA 2950 Thermogravimetric Analyzer from room temperature to 700 $^{\circ}\text{C}$ under nitrogen atmosphere at a heating rate of 10 $^{\circ}\text{C}/\text{min}$.

$\{\text{Zn}_2(\text{NDC})_2(\text{AzoAEpP}) \cdot 2\text{DMF}\}_n$ (ABMOF-1). AzoAEpP (21.1 mg, 50.0 μmol), $\text{Zn}(\text{NO}_3)_2 \cdot 4\text{H}_2\text{O}$ (26.1 mg, 0.100 mmol) and 1,4-naphthalenedicarboxylic acid (NDC, 21.6 mg, 0.100 mmol) were combined in a sealed microwave vial in DMF/ H_2O (6.8 mL/0.2 mL). After the reaction mixture was sonicated for 2 min, the clear solution was subjected to a programmed reaction cycle that involved steady, gradual heating to 100 $^{\circ}\text{C}$ over 1 h, followed by maintaining a constant temperature for 48 h and then gradual cooling to room temperature over 6 h. The resulting orange-red blocks were harvested by filtration, and then washed and stored in DMF. NMR analysis of ABMOF-1 after digestion with D_2SO_4 in DMSO-d_6 was consistent with a 2:1 ratio of NDC:AzoAEpP. Elemental analysis calcd. for activated ABMOF-1 $\text{C}_{50}\text{H}_{38}\text{N}_6\text{O}_8\text{Zn}_2$: C 61.12%, H 3.87%, N 8.56%; Found: C 60.46%, H 3.82%, N 8.46%. FT-IR (diamond-ATR, cm^{-1}) 3396.0, 3069.0, 2924.8, 2357.4, 2336.5, 1665.5, 1638.6, 1620.0, 1595.0, 1576.2, 1501.6, 1468.3, 1427.0, 1369.0, 1315.0, 1263.3, 1248.9, 1227.9, 1215.7, 1192.8, 1161.8, 1124.5, 1093.4, 1072.4, 1035.1, 983.4, 900.6, 863.3, 826.0, 790.6, 767.7, 747.0, 670.5, 655.8. TGA shows a 12.6% weight loss before 190 $^{\circ}\text{C}$, corresponding to the loss encapsulated DMF, and MOF decomposition at 270 $^{\circ}\text{C}$. No weight loss is observed if the ABMOF-1 is pretreated by drying at 80 $^{\circ}\text{C}$ for four h, and decomposition occurs at 270 $^{\circ}\text{C}$.

X-ray Crystallography. Structural analysis was carried out in the X-Ray Crystallographic Facility at Worcester Polytechnic Institute. Crystals were glued on tip of a glass fiber and were

mounted on a Bruker-AXS APEX CCD diffractometer equipped with an LT-II low temperature device. Diffraction data were collected at room temperature or 100 K using graphite monochromated Mo-K α radiation ($\lambda = 0.71073 \text{ \AA}$) using the omega scan technique. Empirical absorption corrections were applied using the SADABS program.²⁶ The unit cells and space groups were determined using the SAINT+ program.²⁶ The structures were solved by direct methods and refined by full matrix least-squares using the SHELXTL program.²⁷ Refinement was based on F^2 using all reflections. All non-hydrogen atoms were refined anisotropically. Hydrogen atoms on carbon atoms were all located in the difference maps and subsequently placed at idealized positions and given isotropic U values 1.2 times that of the carbon atom to which they were bonded. Hydrogen atoms bonded to oxygen atoms were located and refined with isotropic thermal parameters. Mercury 3.1 software was used to examine the molecular structure. Relevant crystallographic information is summarized in Table 1 and Table 2, and the 50% thermal ellipsoid plot is shown in Figure 1.

Powder X-ray Diffraction. PXRD data were collected on a Bruker-AXS D8-Advance diffractometer using Cu-K α radiation with X-rays generated at 40 kV and 40 mA. Bulk samples of crystals were placed in a 20 cm \times 16 cm \times 1 mm well in a glass sample holder, and scanned at RT from 3 $^\circ$ to 50 $^\circ$ (2 θ) in 0.05 $^\circ$ steps at a scan rate of 2 $^\circ$ /min. Simulated PXRD patterns from single crystal data were compared to PXRD patterns of ABMOF-1, to confirm the uniformity of the crystalline sample.

General Spectroscopic Methods. Solution UV-vis absorption spectra were acquired in 1.0 cm quartz cuvettes at room temperature and recorded on a Thermo Scientific Evolution 300 UV-vis spectrometer with inbuilt Cary winUV software. Steady-state diffuse reflectance UV-vis spectra were obtained on the same instrument with a Harrick Praying Mantis diffuse reflectance

accessory (Harrick Scientific Products) and referenced to MgSO_4 .⁴ Solution emission spectra were recorded on a Hitachi F-4500 spectrophotometer with excitation and emission slit widths of 5 nm. The excitation source was a 150 W Xe arc lamp (Ushio Inc.) operating at a current of 5 A and equipped with photomultiplier tube with a power of 400 V. Analytes screened included 2,4-dinitrophenol (2,4-DNP), chlorobenzene (CB), 1,3-dinitrobenzene (1,3-DNB), 1,4-dinitrobenzene (1,4-DNB), 2-nitrophenol (2-NP), 4-nitrophenol (4-NP), and 2,6-dinitro-4-trifluoromethyl phenol (2,6-DNP-4- CF_3).

Emission and Quantum Yield Determination. Steady-state emission were recorded on a Hitachi F-4500 spectrophotometer with excitation and emission slit widths of 5 nm. The excitation source was a 150 W Xe arc lamp (Ushio Inc.) operating at a current of 5 A and equipped with photomultiplier tube at 400 V. Quantum yields in the solid state were determined in triplicated using published procedures with Na_2SO_4 as the reference.^{4, 28}

Analyte Detection by Emission. A 2 mL suspension of powdered ABMOF-1 (40 μM in DMF) was prepared from a 2 mM stock solution and the emission spectra was recorded ($\lambda_{\text{ex}} = 523 \text{ nm}$). For each emission assay, three 40 μL aliquots from 2 mM stock solutions were added successively to obtain the response to 1-10 equivalents of the analyte (1 eq with respect to AzoAEP units) to the ABMOF-1 suspension. After each aliquot addition, the mixture was equilibrated by stirring for 30 min before the emission spectrum was recorded. The emission response to all analytes was measured by integrating the emission band between 530-800 nm. All spectroscopic experiments were performed in triplicate.

X-ray photoelectron spectroscopy. Analyte-MOF samples for XP spectroscopy were specifically limited to the 2,6-DNP-4- CF_3 and ABMOF-1 crystals with 4 mm \times 4 mm faces.

Washing three times in DMF and overnight air drying followed MOF exposure to the DNP-CF₃. A PHI5600 XPS with a third-party acquisition system (RBD Instruments, Bend Oregon) acquired all photoelectron spectra as described previously.²⁹ Analysis chamber base pressures were $<1 \times 10^{-9}$ torr. For certain experiments, argon-ion sputtering removal of near-interfacial species preceded XPS acquisition. With the MOF/analyte sample in the XPS analysis chamber, sputter conditions utilized a differentially pumped ion gun source at 25 mA electron emission, 3.5 kV beam voltage, and $\sim 1.5 \times 10^{-4}$ Torr of research-grade argon. Sputtering lasted for 6 s during which the ion gun rastered the beam across the sample over an area that was aligned with and somewhat larger than the sampling area of the analyzer. A hemispherical energy analyzer that was positioned at 90° with respect to the incoming X-ray flux collected photoelectrons at angles of 30°, 45°, and 60° with respect to the MOF surface normal angle. For the large-faced samples under study, photoelectron acquisition at higher angles with respect to the surface normal demonstrated increased surface sensitivity as compared to acquisition at smaller angles.²³ Survey spectra utilized a pass energy of 117 eV, a 0.5 eV step size, and a 50 ms per step dwell time. High-resolution XP spectra employed a 23.5 eV pass energy, 25 meV step size, and a 50 ms dwell time per step. A low-energy electron gun provided charge neutralization. Neutralization power and energy were optimized to minimize fwhm peak widths rather than to position a peak at a specific binding energy. With features ascribed to adventitious carbon between 283.5–285.0 eV under this neutralization methodology, spectra were linearly shifted to position the adventitious carbon feature at 284.8 eV in the data analysis phase. Data for the Zn 2p_{3/2} photoelectron region were fit with a Shirley-type background,³⁰ and Gaussian-Lorentzian (pseudo-Voigt) GL(30)-style peak shapes.³¹ Universal Tougaard-style backgrounds,³² and GL(30)-style peak shapes described photoelectron features for the C 1s, O 1s, and F 1s regions.

Fits that employ multiple peaks within a spectral region utilized identical fwhm values for each peak to minimize mathematically optimized but potentially chemically unrealistic fits. A substrate overlayer model interprets the fluorine and zinc photoelectron peak area in terms of a fractional coverage of an adsorbed analyte on an idealized ABMOF-1 surface. While the model assumes idealized monodentate coverages that are not directly quantified in the present studies, overlayer coverage interpretations guide qualitative insight into MOF-analyte interactions.

RESULTS AND DISCUSSION

Synthesis and structure. Our previous investigations with silver coordination polymers indicated that AzoAEpP can behave like a rigid, linear bipyridine ligand despite an increased size and flexibility.²⁴ Like many other bipyridine ligands, we did not observe the formation of discrete, well-defined crystalline materials with AzoAEpP and Zn²⁺;³³ however, when used in conjunction with dicarboxylate ligands, AzoAEpP forms pillared paddle-wheel MOFs. Benzene 1,4-dicarboxylic acid (BDC) and 1,4-naphthalenedicarboxylic acid (NDC) form similar structures. In {Zn₂(NDC)₂(AzoAEpP)•2DMF}_n (ABMOF-1), each dinuclear Zn²⁺ site is bridged by a carboxylate from each of four NDC ligands to form paddle-wheel complexes with the second carboxylate from each NDC ligand connecting to an independent Zn²⁺ paddle-wheel unit (Figure 1A). The paddle-wheel coordination polymer sheets are in turn pillared with AzoAEpP ligands to form a three-dimensional framework. The basic structure, as well as the accompanying paddle wheel geometry and bond distances are comparable to those found in other pillared paddle-wheel MOFs.³⁴⁻³⁶ The coordination chemistry in {Zn₂(BDC)₂(AzoAEpP)•2DMF}_n (ABMOF-2) is identical to that of ABMOF-1.

Unlike linear bipyridine ligands like 4,4'-bipyridine, AzoAEP can reorient by rotation of the phenyl–azo C–N bonds, anilino–ethylene N–C bonds, ethylene–pyridine C–C bonds and/or the ethylene bonds C–C. The multiple degrees of freedom enable AzoAEP to adopt structures that differ from those accessible with rigid ligands. Owing to the nonlinear shape of AzoAEP, the ABMOF-1 framework forms a tilted primitive cubic net (Figure 1B), in contrast to the frequently observed vertical³³ or semi-vertical cubic nets.³⁴ The use of extended dicarboxylate ligands or bidentate pillars often leads to multiply interpenetrated frameworks.^{34, 37} ABMOF-2 forms a 3-fold interpenetrated framework, with a vertical primitive cubic net whereas ABMOF-1 forms a non-interpenetrated framework with permanent porosity. Although the dicarboxylate span of NDC and BDC is similar, the point-to-point distance between the two pyridine nitrogen atoms of AzoAEP in ABMOF-1 and ABMOF-2 frameworks is quite different, 13.0 Å and 19.3 Å respectively. Furthermore, the effective distance in ABMOF-1 obtained by projecting one pyridine nitrogen on a plane containing the other pyridine is even shorter, 7.1 Å in ABMOF-1 compared to 19.3 Å in ABMOF-2 where the pyridine ligands are collinear. The linear conformation in AzoAEP in ABMOF-2 opens enough void space to permit 3-fold interpenetration. Compared to the structure of the apo ligand, in ABMOF-1, the azo N–C bonds rotate by 180°, anilino–ethylene N–C bonds rotate by 65°, and ethylene–pyridine C–C rotates 71°, resulting in the lone pairs pointing toward the diazene core as opposed to outward in the free ligand. This results in primitive cubic net where framework interpenetration is blocked by the ligands occupying the void space.

Examination of ABMOF-1 crystal structure reveals one-dimensional pores along *c* axis of with an average size of $4.5 \times 1.9 \text{ \AA}^2$, after removing DMF guest molecules (Figure 1C). PLATON analysis using SQUEEZE³⁸ shows an average solvent accessible size of $4.5 \times 1.8 \text{ \AA}^2$,

with the void space occupying 26.2% of the total volume. The pore-size cannot be measured precisely in ABMOF-2 due to crystallographic disorder in the azobenzene ligand; however, the pores are smaller and interpenetration further restricts the void space. The pores in ABMOF-1 are relatively small, especially for a non-interpenetrated network. Interpenetrated pillared paddlewheel MOFs tend to contain pores with dimensions not much larger than 5 Å,³⁹ whereas non-interpenetrated pillared paddlewheel MOFs contain larger pores with dimensions between 11–40 Å.⁴⁰⁻⁴² Non-interpenetrated MOFs with large pores can encapsulate large molecules such as ibuprofen,⁴³ benzene,⁴⁴ or toluene,⁴⁵ whereas interpenetrated MOFs are usually limited to small molecules such as CO₂⁴⁶ and other gases.⁴⁷ Despite having a non-interpenetrated structure, the small pores in ABMOF-1 preclude the inclusion of large guest molecules such as the 2,4-dinitrophenol (6.2 × 5.0 Å²). The size exclusion phenomenon has also been shown in other luminescent MOF based detecting systems.^{2, 6, 10}

Photophysical properties of ABMOF-1 and analyte detection. ABMOF-1 exhibits maximum absorbance at 500 nm with a broad emission centered at 610 nm (Figure 2), which are nearly identical to the optical properties observed for Ag⁺ metal organic polymers containing the AzoAEP ligand.²⁴ Our investigations also demonstrated that AzoAEP emits with a λ_{\max} at 605 nm when frozen in a solvent glass at 77 K, therefore, we attribute the emission observed in ABMOF-1 to the AzoAEP ligand, since NDC ligand emits at 480 nm. Although the quantum yield is low ($\Phi = 0.4\%$), the emission is clearly visible when ABMOF-1 is dispersed in solvent (Figure 2, inset). Both ABMOF-1 and ABMOF-2 ($\Phi = 0.4\%$) show strong emission at room temperature, but the latter was not responsive to any of the quenchers we screened, so additional studies focused exclusively on ABMOF-1. Since interpenetration is the only significant different between ABMOF-1 and ABMOF-2 and interpenetrated MOFs can be quenched by nitroaromatic

analytes,^{48, 49} we hypothesize that differences in the exposed surface leads to different adsorbate interactions and therefore a contrasting luminescence response, but no definitive conclusion can be made based our experiments thus far.

When dispersed in DMF, powdered ABMOF-1 forms a semi-homogeneous suspension that persists indefinitely without any evidence of decomplexation even after 2 h of sonication. Based on previous studies of emissive MOF quenching,^{2, 9} we chose 6 analytes – chlorobenzene (CB), 1,3-dinitrobenzene (1,3-DNB), 1,4-diiobenzene (1,4-DIB), 2-nitrophenol (2-NP), 4-nitrophenol (4-NP) and 2,4-dinitrophenol (2,4-DNP) – to probe the quenching response of ABMOF-1. All the aryl molecules can potentially π -stack with the aromatic MOF struts, but only the phenolic analytes can engage in electrostatic interactions with charged MOF components. Electron-deficient aromatic compounds readily quench MOF emission, so analytes were also chosen to probe the scope of this behavior. The aromatic substituents range from inductively withdrawing halides to nitro groups, which are strongly electron withdrawing by resonance. Trinitroaromatics, which are typically the strongest quenching species, were not screened owing to associated hazards.

Of all the analytes screened, only 2,4-DNP quenched ABMOF-1 emission significantly (Figure 3). We attribute this response primarily to the proximity of the analyte to chromophores on or near the MOF surface since the spherical diameter of 2,4-DNP (7 Å) is larger than the pores in ABMOF-1. Nitroaromatic compounds typically quench emission by an electron transfer process from an electronically excited chromophore coming into a low-lying empty orbital on the nitro compound, which is also true of MOFs.⁴⁸⁻⁵⁰ Although we cannot completely exclude energy-transfer quenching mechanisms observed in some MOF systems^{2, 51} the lack of spectral overlap between emission spectra of ABMOF-1 and absorption spectra of the analyte suggests

the contributions from these alternative pathways is minimal. The absence of emission peak shifting characteristic of energy transfer also support this conclusion.

Achieving a significant emission response in ABMOF-1 requires a strong quencher with a low lying LUMO, and a phenol to decrease the distance between fluorophore and quencher, which is consistent with the proposed electron transfer quenching mechanism. In ABMOF-1, the quenching response to 2-NP (approximately 20% reduction in integrated emission) and 4-NP (approximately 25%) is minimal, whereas 2,4-DNP quenches almost completely (97%). The lack of emission quenching with 1,3-DNB, suggests the hydroxyl of 2,4-DNP anchors the analyte to the MOF surface either through an interaction with surface-exposed Zn^{2+} ions, carboxylic acids or pyridine groups. A preliminary examination of the Stern-Volmer relationship suggests a shift from dynamic to static quenching as the 2,4-DNP concentration increases. These observations are indicative of a distance-sensitive process like electron transfer, and the quenching properties of 2,4-DNP. Any metal bond to or salt bridge with the weakly coordinating 2,4-DNP anion would be weak and require high concentrations to drive the binding equilibrium. The stronger response to the most electron deficient analyte also supports the conclusion that electron transfer from the electronically excited MOF to a low-lying empty analyte orbital dominates the quenching mechanism.

The narrow channels in ABMOF-1 restrict the MOF-analyte behavior to surface interactions, but obtaining direct evidence to clearly confirm surface adsorption remains difficult. In MOFs with larger pores distinguishing between guests internalized in pores and surface adsorbates imposes an even greater challenge. In ABMOF-1 internalized DMF molecules are observed in the X-ray structure, but surface molecules are outside the detection window, even if those molecules were densely populated, strongly adhered, and sufficiently ordered for

crystallography. MOF emission can be quenched at significantly less than total theoretical pore occupancy,^{52, 53} which excludes detection by single crystal analysis. In contrast, PXRD is sensitive to sample crystallinity changes, but detailed MOF structural information is both difficult to extrapolate, and neither internalized guests nor surface adsorbates necessarily perturb the crystal form.^{48, 49}

In contrast to other X-ray techniques, our XPS measurements were readily able to elucidate interactions between the analytes and ABMOF-1. For an ABMOF-1 sample that was exposed to 2,4-DNP, the XPS spectra revealed no features above a background signal in the portion of the N 1s region that would be ascribable to the nitro groups of the analyte. Separately, we observed rapid sublimation of 2,4-DNP under analogous vacuum conditions similar to those encountered in the XPS load lock. The rapid sublimation 2,4-DNP, and the of lack of observable, unique chemical states for 2,4-DNP-treated ABMOF-1 implies only weak physisorption of the analyte but cannot provide insight into adsorption vs intercalation behavior. As the 2,4-DNP did not demonstrate sufficiently strong interactions with the ABMOF-1 substrate, we explored other emission-quenching analytes with unique chemical features for photoelectron analyses.

Unlike 2,4-DNP, 2,6-DNP-4-CF₃ does not desorb from ABMOF-1 under vacuum and is detectable with photoelectron spectroscopy. Identically to 2,4-DNP however, 2,6-DNP-4-CF₃ quenches ABMOF-1 emission and does not perturb the ABMOF-1 structure as determined by PXRD. By inducing a similar luminescent response while containing three fluorine atoms per molecule that impart an intense and chemically distinct signal in photoelectron spectra,²⁵ 2,6-DNP-4-CF₃ provides a convenient and attractive species to probe adsorption vs intercalation interactions with ABMOF-1.

The high-resolution XP spectra of ABMOF-1 in the absence or presence of 2,6-DNP-4- CF_3 exhibit distinct peaks characteristic of the elemental composition (Figure 4). Each spectrum displays the experimentally measured peaks corresponding to electrons originating from the Zn $2p_{3/2}$, F 1s, N 1s, and C 1s regions (black) and the modeled fits of the data (red). Spectra of analyte-free ABMOF-1 reveal features attributed to Zn^{2+} at ~ 1021 eV, the azo nitrogen atoms at ~ 400 eV, and carboxylate carbon atoms at ~ 289 eV; whereas, only non-fittable background signal were observed in the F 1s region (Figure 4A). Each of the largest fitted peaks corresponding to the Zn $2p_{3/2}$, N 1s, and C 1s regions also possess a smaller satellite feature at an approximately 3 eV lower binding energy with comparable area ratios to each of the large fitted peaks. We ascribe each of these satellites to an artifact of non-homogeneous charging on the ABMOF-1 surface that results in a similarly non-homogeneous charge compensation by the neutralizer. Therefore, the satellite features do not represent distinct chemical features in the photoelectron spectra. Both the aromatic carbon atoms and adventitiously adsorbed carbon species contribute to the large feature in the C 1s region in a manner that prohibits rigorous interpretation.

Upon the introduction of 2,6-DNP-4- CF_3 , the spectra of ABMOF-1 no longer contains the charging artifacts present in the analyte-free spectra; however, the spectra do exhibit features ascribable to the analyte (Figure 4B). Specifically, the F 1s region shows a strong feature due to photoelectron emission from the three fluorine atoms on the trifluoromethyl group of the analyte. Similarly, the N 1s spectrum reveals a feature towards higher binding energy at ~ 406.5 that we assign to the nitro-group nitrogen atoms of 2,6-DNP-4- CF_3 . In addition to these new features, the fluorine atoms in the $-\text{CF}_3$ moiety shift the photoelectron emission corresponding to that carbon atom towards higher binding energy as revealed by the small feature at approximately 292.5 eV

in the C 1s spectrum. Collectively, these results demonstrate an association between the 2,6-DNP-4-CF₃ and the ABMOF-1 substrate; however, further photoelectron analyses are required to elucidate the adsorption vs intercalation nature of the interaction.

Both the Zn 2p_{3/2} and F 1s regions in the spectra of 2,6-DNP-4-CF₃-exposed ABMOF-1 change noticeably due to collection of the photoelectrons at different angles, and following argon-ion sputtering. Figure 5 shows spectra that are representative of acquisitions on multiple 2,6-DNP-4-CF₃-exposed ABMOF-1 samples. The blue traces in both frames represent photoelectron signals collected at 30° with respect to the surface normal angle while the red traces represent signals collected at 60° for 2,6-DNP-4-CF₃-exposed ABMOF-1 samples. Since the probability for photoelectron escape—given by an attenuation length that is related to the inelastic mean free path—decreases exponentially with depth below the sample surface, the electrons generated more deeply in the sample have a decreased probability of reaching the detector relative to electrons generated at shallow depths.²³ When photoelectrons are collected at higher angles with respect to the surface normal, they must travel through more material to escape and have a decreased probability of escape relative to electrons collected at angles closer to the surface normal. Thus, the spectra collected at 30° are more sensitive to content of the bulk material when compared to spectra that are collected at 60°, which are more surface sensitive. Considering a ratio of area intensities for the F 1s that is a proxy for 2,6-DNP-4-CF₃ and the Zn 2p_{3/2} intensity that is a proxy for ABMOF-1, an $I_{F\ 1s}/I_{Zn\ 2p_{3/2}}$ ratio would demonstrate no angle dependence for homogeneously intercalated guests while the ratio would increase with increasing angle for surface-adsorbates. The photoelectron spectra collected at 30° in Fig. 5 (blue) demonstrate $I_{F\ 1s}/I_{Zn\ 2p_{3/2}} = 857\ \text{cps} / 1178\ \text{cps} = 0.73$, while the spectra collected at 60° (red) demonstrate $I_{F\ 1s}/I_{Zn\ 2p_{3/2}} = 403\ \text{cps} / 382\ \text{cps} = 1.1$. The increase in the F 1s-to-Zn 2p_{3/2}

peak area ratio at 60° relative to 30° indicates that the fluorine atoms are physically situated closer to the sample surface relative to the Zn²⁺ atoms.

Photoelectron scans following argon-ion sputtering further reveal the physical relationship between the fluorine atoms and the Zn²⁺ atoms (Figure 5). Sputter conditions yield a sample bombardment of 3.5 keV Ar⁺ ions for six seconds. Calibration studies from our lab indicate that these sputtering conditions remove approximately 2–5 monolayers of adsorbed species on substrates under study. The resulting Zn 2p_{3/2} trace (black) following Ar⁺ sputtering demonstrates a significantly larger intensity compared to the Zn 2p_{3/2} features collected at either 30° or 60° in the absence of sputter cleaning. In contrast to the Zn 2p_{3/2} signals, the resulting F 1s signals following sputtering are greatly attenuated relative to the F 1s data collected at 30° or 60° in the absence of sputtering. The increase of the Zn 2p_{3/2} suggests the removal of species above the layer that contains the Zn²⁺ atoms, which had attenuated the Zn 2p_{3/2} signals before sputtering. The decrease of the F 1s signal indicates the fluorine atoms were principally localized in the top 2–5 monolayers of species that were sputtered away due to Ar⁺ bombardment; therefore, the combination of angle-resolved XPS and argon-ion sputtering results reveal that the fluorine atoms are localized in the near interfacial layers of the sample, while the Zn²⁺ atoms are localized in the bulk material.

A model consistent with the photoelectron data is the surface adsorption of 2,6-DNP-4-CF₃ on the ABMOF–1 substrate. If the analyte had intercalated into the ABMOF–1 network, we would have observed no relative change in the Zn²⁺ to fluorine signals. Based on analyte adsorption, we utilize substrate overlayer models to interpret the photoelectron data in terms of a relative surface coverage of the 2,6-DNP-4-CF₃ analytes on the ABMOF–1 surface.⁵⁴⁻⁵⁷ We model the adsorption of individual 2,6-DNP-4-CF₃ molecules per surface-available Zn²⁺ species,

for which we employ two surface-available Zn^{2+} sites per unit cell (100) face based on the from the XRD results above. For the photoelectron data collected at 45° with respect to a surface normal, three separate samples yielded a F 1s-to-Zn $2p_{3/2}$ peak area ratio of 0.68 ± 0.02 corresponding to a surface coverage of $100 \pm 2\%$. While overlayer model results may imply ideal monolayer coverage of adsorbed 2,6-DNP-4- CF_3 analytes, the precise mode of adsorption and the density of surface-available zinc cations remain the subject of ongoing study in our laboratory. Rather, the XPS and coverage calculations to imply strong adsorption of particular nitrophenol species with generally high coverage of ABMOF-1 surfaces that validates the use of photoelectron spectroscopy for elucidating the role of this analyte-MOF interaction.

CONCLUSIONS

Embedding azobenzene struts into rigid MOF structures can lead to emission from the chromophore instead of dissipation of excitation energy via non-radiative pathways. ABMOF-1 and ABMOF-2 are the first emissive MOFs containing azobenzene fluorophores, but only ABMOF-1 responds significantly to various nitroaromatic analytes. Based on the similarity of the emission response to other luminescent MOF systems and the pore sizes that preclude guest encapsulation, we reasoned that ABMOF-1 would be a valuable test case to evaluate XPS as an analytical technique to detect surface adsorbed species. Different from optical spectroscopies and other techniques, the interfacial sensitivity of XPS can elucidate the presence specific chemical species and states on a material surface with a sub-monolayer limit of detection. Although we are conducting additional studies understand the atomic level interactions at the surface, an association between the analyte and the ABMOF-1 substrate has been demonstrated by high-

resolution XPS showing strong features of adsorbate-associated fluorine atoms, as well as the energy level shifting of nitrogen and carbon photoelectron emission, sustaining as a novel way to characterize surface-associated nitroaromatic analytes on MOFs. Angle-resolved and argon-ion sputtering XPS further indicate analytes are physically situated closer to the sample surface. The study of MOF-analyte interactions by collecting XPS data at different angles and sputtering several surface monolayers provide a new method to study interactions in MOFs or other coordination polymers.

ACKNOWLEDGMENT

We thank Prof. Christopher Lambert for guidance with diffuse reflectance and solid-state emission measurements. This work was supported by the American Chemical Society Petroleum Research Fund grant 53977-ND3 and Worcester Polytechnic Institute.

Table 1. Crystal data and structure refinements for ABMOF-1.

Compound	{Zn ₂ (NDC) ₂ (AzoAEP) • 2DMF} _n
Formula	C ₅₆ H ₅₂ N ₈ O ₁₀ Zn ₂
Formula weight (g mol ⁻¹)	1127.84
Crystal size	1.00 × 0.75 × 0.15
Crystal system	Monoclinic
Color	Orange-red
Space group	P2 ₁ /c
a/Å	12.1475
b/Å	15.602
c/Å	14.578
α/°	90.00
β/°	99.566
γ/°	90.00
Volume/Å ³	2724.5
Z	4
Temp, K	296 (2)
ρ _{calc} /cm ³	1.375
Radiation	Mo Kα (λ = 0.71073 Å)
2θ range for data collection/°	4.82 to 66.26
Index ranges	-18 ≤ h ≤ 18, -23 ≤ k ≤ 23, -19 ≤ l ≤ 22
Reflections collected	39345
Independent reflections	10334
Observed reflections	8084
R	0.0403
wR2	0.1439
no. of parameters	345
Goodness-of-fit on F2	1.056

Table 2. Crystal data and structure refinements for ABMOF-2.

Compound	$\{Zn_2(BDC)_2(AzoAEPpP)\}_n$
Formula	$C_{50}H_{40}N_6O_8Zn$
Formula weight (g mol ⁻¹)	918.25
Crystal size	0.25 × 0.18 × 0.01
Crystal system	Monoclinic
Color	Orange
Space group	C 1 2/m 1
a/Å	15.730(3)
b/Å	15.100(3)
c/Å	10.023(2)
α/°	90.00
β/°	119.21(3)
γ/°	90.00
Volume/Å ³	2078.0(9)
Z	2
Temp, K	100 (2)
ρ _{calc} /cm ³	1.468
Radiation	Mo Kα (λ = 0.71073Å)
2θ range for data collection/°	4.92 to 46.36
Index ranges	-20 ≤ h ≤ 20, -16 ≤ k ≤ 19, -12 ≤ l ≤ 12
Reflections collected	11989
Independent reflections	2357
Observed reflections	1825
R	0.0521
wR2	0.1397
no. of parameters	344
Goodness-of-fit on F2	1.090

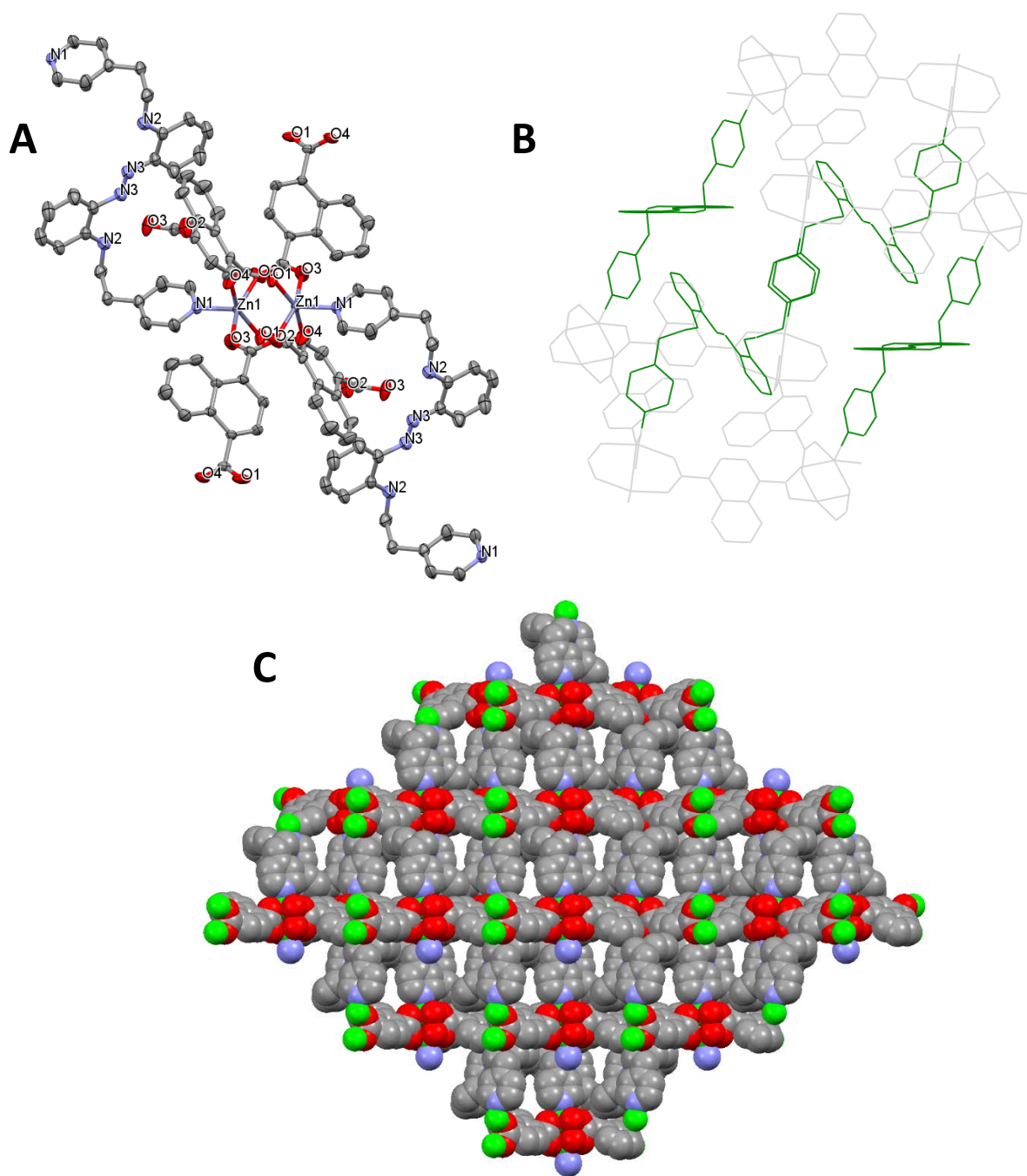


Figure 1A. Thermal ellipsoid representation of ABMOF-1 showing atoms at 50% probability levels, and selected atom labels. Hydrogen atoms are omitted for clarity. **1B** Wireframe diagram of ABMOF-1 showing primitive cubic nets with four AzoAEP ligand pillars in green. **1C** Space-filling diagram of ABMOF-1 showing crystal packing of the non-interpenetrated MOF structure showing the pore structure. Zn = green, N = blue, O = red, and C = gray. Hydrogen atoms and DMF molecules have been omitted for clarity.

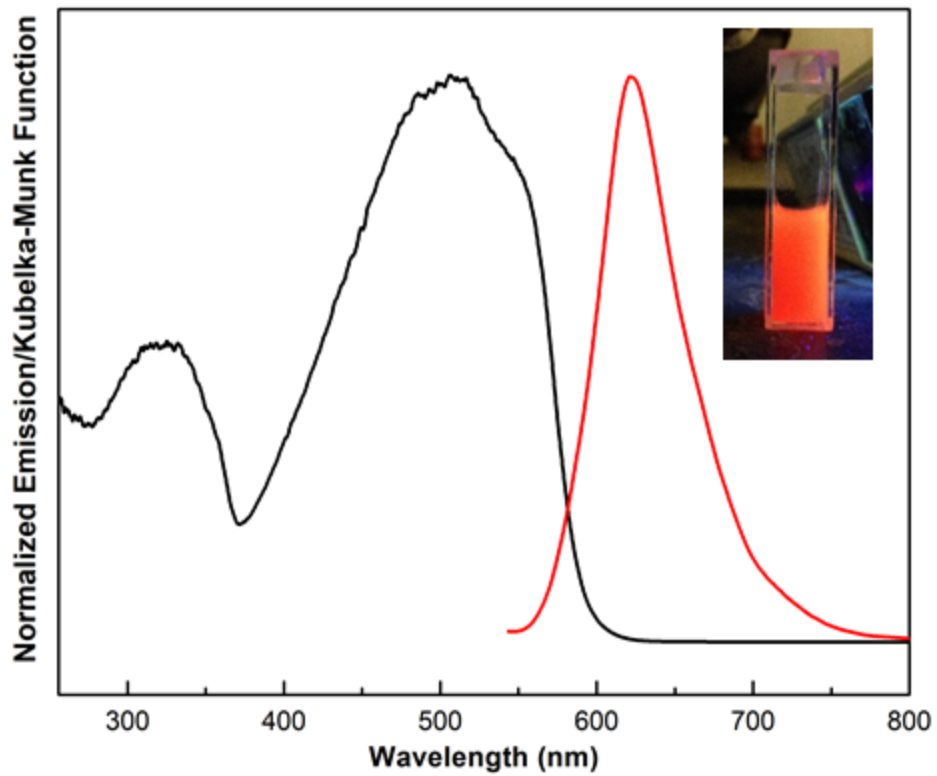


Figure 2. Solid state diffuse reflectance (black) and solid state emission ($\lambda_{\text{ex}} = 523$ nm, red) spectra of ABMOF-1.

Inset: cuvettes containing a suspension of the complex crystals in DMF (40 μM) excited with 365 nm light (right).

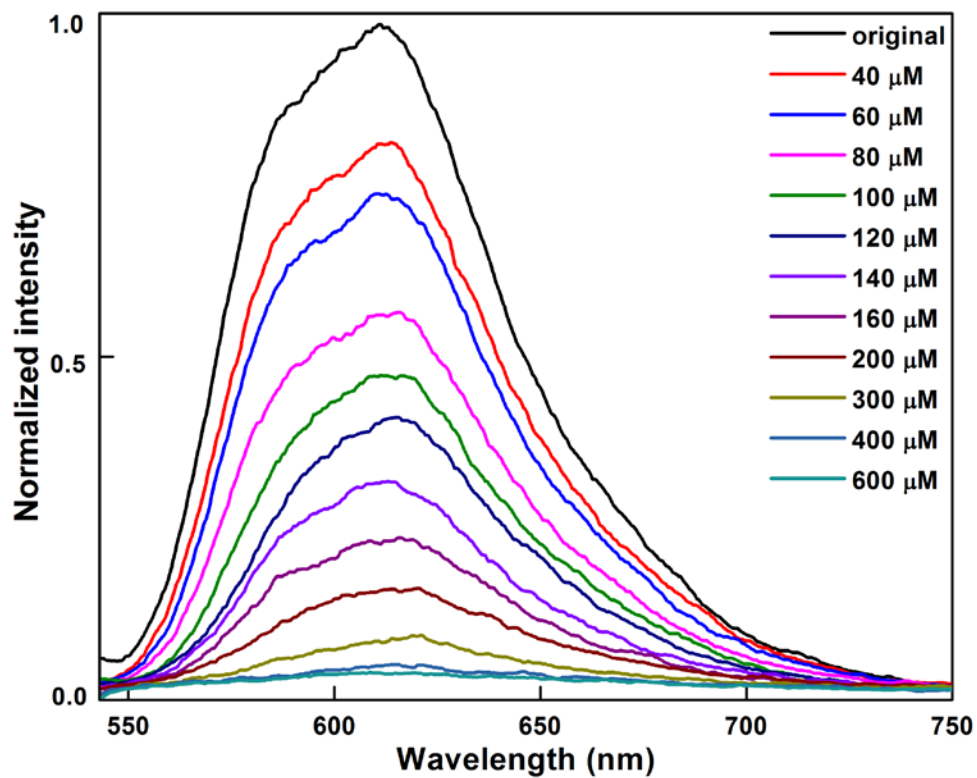


Figure 3. Normalized emission response of ABMOF-1 to 2,4-DNP ($\lambda_{\text{ex}} = 523 \text{ nm}$). ABMOF-1 ($40 \mu\text{M}$) was suspended in DMF (black) and treated with 2,4-DNP in DMF to obtain final concentration of $40 \mu\text{M}$, $80 \mu\text{M}$, $120 \mu\text{M}$, $160 \mu\text{M}$, $200 \mu\text{M}$, until $600 \mu\text{M}$. Solutions were equilibrated for 30 min before each measurement.

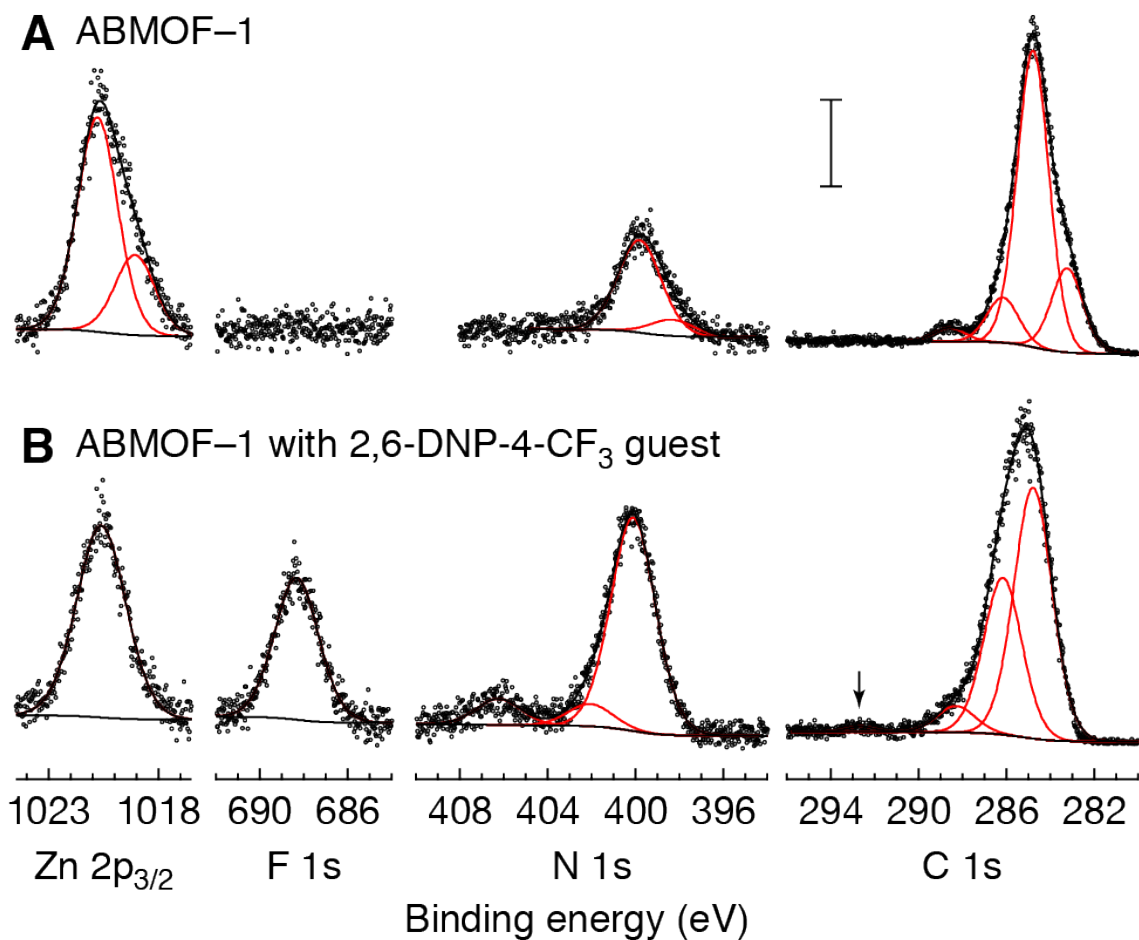


Figure 4. XP spectra of representative ABMOF-1 samples both (A) with no analyte exposure, and (B) following exposure to 2,6-dinitro-4-trifluoromethyl-phenol (2,6-DNP-4-CF₃). The F 1s region demonstrates no visible features for a non-exposed sample and strong features ascribed to fluorine in the CF₃ group for the ABMOF-1 following 2,6-DNP-4-CF₃ exposure. Additional features in frame B include a N 1s feature ascribed to a nitro species at 406.5 eV and a C 1s feature due to carbon in a CF₃ group at 292.5 eV (arrow). The vertical scale bar represents 100 counts per second (cps) for the Zn 2p_{3/2}, F 1s, and N 1s regions, and 300 cps for the C 1s regions in both frames. We attribute to the satellite fits in frame A to non-homogeneous charge neutralization of the insulating MOF sample.

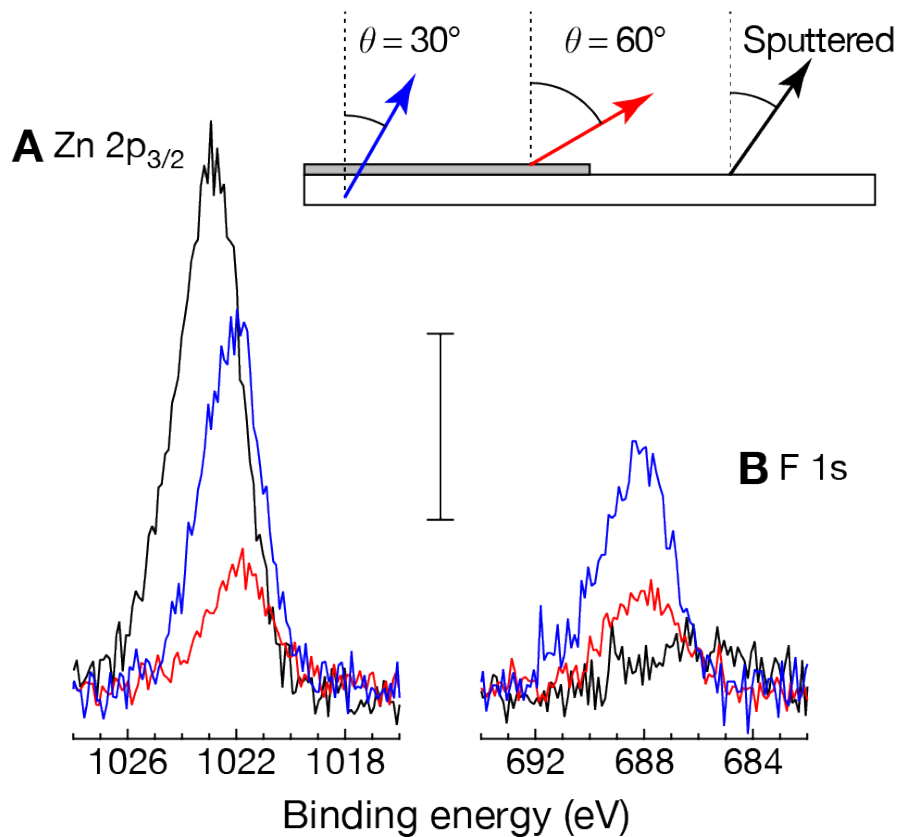


Figure 5. XP spectra of the (A) Zn $2p_{3/2}$, and (B) F 1s regions for ABMOF-1 samples exposed to 2,6-DNP-4- CF_3 . In both frames, the blue traces correspond to photoelectron take-off angles of 30° with respect to the surface normal that is a comparatively bulk-sensitive angle. The red traces correspond to photoelectron take-off angles of 60° , which is a more surface-sensitive angle as compared to the 30° results. Lastly, the black traces correspond to photoelectron signals following a brief argon-ion sputter to remove near-interfacial species. This combination of results demonstrates that the signals due to fluorine are present closer to the sample surface relative to the signals due to Zn^{2+} . We interpret the more surface-localized nature of the fluorine signals to result from 2,6-DNP-4- CF_3 that is adsorbed onto rather than intercalated into the ABMOF-1 substrate. The scale bar represents 100 cps for both frames.

REFERENCES

1. A. J. Lan, K. H. Li, H. H. Wu, D. H. Olson, T. J. Emge, W. Ki, M. C. Hong and J. Li, *Angew. Chem. Int. Edit.* 2009, **48**, 2334-2338.
2. S. S. Nagarkar, B. Joarder, A. K. Chaudhari, S. Mukherjee and S. K. Ghosh, *Angew. Chem. Int. Edit.* 2013, **52**, 2881-2885.
3. Z. C. Hu, B. J. Deibert and J. Li, *Chem. Soc. Rev.* 2014, **43**, 5815-5840.
4. N. B. Shustova, B. D. McCarthy and M. Dinca, *J. Am. Chem. Soc.* 2011, **133**, 20126-20129.
5. C. Y. Lee, O. K. Farha, B. J. Hong, A. A. Sarjeant, S. T. Nguyen and J. T. Hupp, *J. Am. Chem. Soc.* 2011, **133**, 15858-15861.
6. B. Gole, A. K. Bar and P. S. Mukherjee, *Chem. Commun.* 2011, **47**, 12137-12139.
7. Z. Z. Lu, R. Zhang, Y. Z. Li, Z. J. Guo and H. G. Zheng, *J. Am. Chem. Soc.* 2011, **133**, 4172-4174.
8. X. Q. Zou, G. S. Zhu, I. J. Hewitt, F. X. Sun and S. L. Qiu, *Dalton Trans.* 2009, DOI: 10.1039/b822248g, 3009-3013.
9. Z. J. Zhang, S. C. Xiang, X. T. Rao, Q. A. Zheng, F. R. Fronczek, G. D. Qian and B. L. Chen, *Chem. Commun.* 2010, **46**, 7205-7207.
10. D. Tian, Y. Li, R. Y. Chen, Z. Chang, G. Y. Wang and X. H. Bu, *J. Mater. Chem. A* 2014, **2**, 1465-1470.
11. S. Shimomura, S. Horike, R. Matsuda and S. Kitagawa, *J. Am. Chem. Soc.* 2007, **129**, 10990-+.
12. L. Alaerts, C. E. A. Kirschhock, M. Maes, M. A. van der Veen, V. Finsy, A. Depla, J. A. Martens, G. V. Baron, P. A. Jacobs, J. E. M. Denayer and D. E. De Vos, *Angew. Chem. Int. Edit.* 2007, **46**, 4293-4297.
13. X. Lin, A. J. Blake, C. Wilson, X. Z. Sun, N. R. Champness, M. W. George, P. Hubberstey, R. Mokaya and M. Schroder, *J. Am. Chem. Soc.* 2006, **128**, 10745-10753.
14. Y. Takashima, V. M. Martinez, S. Furukawa, M. Kondo, S. Shimomura, H. Uehara, M. Nakahama, K. Sugimoto and S. Kitagawa, *Nat. Commun.* 2011, **2**.
15. Z. X. Zhao, X. M. Li, S. S. Huang, Q. B. Xia and Z. Li, *Ind. Eng. Chem. Res.* 2011, **50**, 2254-2261.
16. J. A. Greathouse, N. W. Ockwig, L. J. Criscenti, T. R. Guilinger, P. Pohl and M. D. Allendorf, *Phys. Chem. Chem. Phys.* 2010, **12**, 12621-12629.
17. G. H. Gao, S. J. Li, S. Li, Y. D. Wang, P. Zhao, X. Y. Zhang and X. H. Hou, *Talanta* 2018, **180**, 358-367.
18. X. L. Zhao, S. L. Liu, Z. Tang, H. Y. Niu, Y. Q. Cai, W. Meng, F. C. Wu and J. P. Giesy, *Sci. Rep.* 2015, **5**.
19. A. S. Duke, E. A. Dolgoplova, R. P. Galhenage, S. C. Ammal, A. Heyden, M. D. Smith, D. A. Chen and N. B. Shustova, *J. Phys. Chem. C* 2015, **119**, 27457-27466.
20. A. Taher, D. W. Kim and I. M. Lee, *RSC Adv.* 2017, **7**, 17806-17812.
21. L. Shi, T. Wang, H. B. Zhang, K. Chang, X. G. Meng, H. M. Liu and J. H. Ye, *Adv. Sci.* 2015, **2**.
22. M. F. Ebel, *J. Electron Spectrosc.* 1978, **14**, 287-322.
23. C. S. Fadley, *Prog. Solid State Chem.* 1976, **11**, 265-343.
24. J. J. W. Yan, L.; Basa, P. N.; Shuettel, M.; MacDonald, J. C.; Ciofini, I.; Coudert, F. X.; Burdette, S. C., *Manuscript submitted* 2018.

25. J. F. S. Moulder, W. F.; Sobol, P. E.; Bomben, K. D., *Handbook of X-ray Photoelectron Spectroscopy*, Physical Electronics Division: Perkin-Elmer Corporation, Eden Prairie, MN, 1992.
26. G. M. Sheldrick, *SADABS*, University of Göttingen, Göttingen, Germany, 1996.
27. G. M. Sheldrick, *Acta Crystallogr. C Struct. Chem.* 2015, **71**, 3-8.
28. M. S. Wrighton, D. S. Ginley and D. L. Morse, *J. Phys. Chem.* 1974, **78**, 2229-2233.
29. A. D. Carl, R. E. Kalan, J. D. Obayemi, M. G. Z. Kana, W. O. Soboyejo and R. L. Grimm, *ACS Appl. Mater. Inter.* 2017, **9**, 34377-34388.
30. D. A. Shirley, *Phys. Rev. B* 1972, **5**, 4709-&.
31. N. Fairley, http://www.casaxps.com/help_manual/manual_updates/peak_fitting_in_xps.pdf (accessed May 18 2017).
32. S. Tougaard, *Surf. Interface Anal.* 1997, **25**, 137-154.
33. B. Q. Ma, K. L. Mulfort and J. T. Hupp, *Inorg. Chem.* 2005, **44**, 4912-4914.
34. B. L. Chen, S. Q. Ma, E. J. Hurtado, E. B. Lobkovsky and H. C. Zhou, *Inorg. Chem.* 2007, **46**, 8490-8492.
35. T. Gadzikwa, O. K. Farha, K. L. Mulfort, J. T. Hupp and S. T. Nguyen, *Chem. Commun.* 2009, DOI: 10.1039/b823392f, 3720-3722.
36. W. Bury, D. Fairen-Jimenez, M. B. Lalonde, R. Q. Snurr, O. K. Farha and J. T. Hupp, *Chem. Mater.* 2013, **25**, 739-744.
37. B. Kesanli, Y. Cui, M. R. Smith, E. W. Bittner, B. C. Bockrath and W. B. Lin, *Angew. Chem. Int. Edit.* 2005, **44**, 72-75.
38. A. L. Spek, *J. Appl. Crystallogr.* 2003, **36**, 7-13.
39. B. L. Chen, C. D. Liang, J. Yang, D. S. Contreras, Y. L. Clancy, E. B. Lobkovsky, O. M. Yaghi and S. Dai, *Angew. Chem. Int. Edit.* 2006, **45**, 1390-1393.
40. P. Horcajada, C. Serre, M. Vallet-Regi, M. Sebban, F. Taulelle and G. Ferey, *Angew. Chem. Int. Edit.* 2006, **45**, 5974-5978.
41. H. Chun, D. N. Dybtsev, H. Kim and K. Kim, *Chem. Eur. J.* 2005, **11**, 3521-3529.
42. A. M. Shultz, O. K. Farha, J. T. Hupp and S. T. Nguyen, *J. Am. Chem. Soc.* 2009, **131**, 4204-+.
43. K. J. Hartlieb, D. P. Ferris, J. M. Holcroft, I. Kandela, C. L. Stern, M. S. Nassar, Y. Y. Botros and J. F. Stoddart, *Mol. Pharmaceut.* 2017, **14**, 1831-1839.
44. A. Santra, M. Francis, S. Parshamoni and S. Konar, *Chemistryselect* 2017, **2**, 3200-3206.
45. W. P. Qin, W. X. Cao, H. L. Liu, Z. Li and Y. W. Li, *RSC Adv.* 2014, **4**, 2414-2420.
46. B. Ugale, S. S. Dhankhar and C. M. Nagaraja, *Cryst. Growth Des.* 2017, **17**, 3295-3305.
47. J. F. Cai, J. C. Yu, H. Xu, Y. B. He, X. Duan, Y. J. Cui, C. D. Wu, B. L. Chen and G. D. Qian, *Cryst. Growth Des.* 2013, **13**, 2094-2097.
48. K. S. Asha, K. Bhattacharyya and S. Mandal, *J. Mater. Chem. C* 2014, **2**, 10073-10081.
49. X. Li, L. Yang, L. Zhao, X. L. Wang, K. Z. Shao and Z. M. Su, *Cryst. Growth Des.* 2016, **16**, 4374-4382.
50. X. Z. Song, S. Y. Song, S. N. Zhao, Z. M. Hao, M. Zhu, X. Meng, L. L. Wu and H. J. Zhang, *Adv. Funct. Mater.* 2014, **24**, 4034-4041.
51. S. S. Nagarkar, A. V. Desai and S. K. Ghosh, *Chem. Commun.* 2014, **50**, 8915-8918.
52. M. H. Zhang, L. L. Zhang, Z. Y. Xiao, Q. H. Zhang, R. M. Wang, F. N. Dai and D. F. Sun, *Sci. Rep.* 2016, **6**.
53. D. Banerjee, Z. C. Hu and J. Li, *Dalton Trans.* 2014, **43**, 10668-10685.

54. J. Chen, S. K. Iyemperumal, T. Fenton, A. D. Carl, R. L. Grimm, G. Li and N. A. Deskins, *ACS Catal.* 2018.
55. M. F. Ebel, *J. Electron Spectrosc.* 1978, **14**, 287-322.
56. W. Gao, K. Zielinski, B. N. Drury, A. D. Carl and R. L. Grimm, *J. Phys. Chem. C* 2018, **122**, 17882-17894.
57. A. Ghosh, L. Gerenser, C. Jarman and J. Fornalik, *Appl. Phys. Lett.* 2005, **86**, 223503.